



作者基于随机合成的图像数据训练了物理信息融合卷积神经网络，以预测激光粉末床熔融过程中打印金属零件的三维温度场变化。然而，该工作没有考虑成形过程材料属性的非线性变化，同时预测结果的时空分辨率较低，只针对结构简单的块体零件进行了研究。

Jiangce Chen

Department of Mechanical Engineering,
Carnegie Mellon University,
Pittsburgh, PA 15213
e-mail: jiangcec@andrew.cmu.edu

Justin Pierce

Fabric8Labs,
San Diego, CA 92121
e-mail: justin.pierce@fabric8labs.com

Glen Williams

Re:Build Manufacturing,
Framingham, MA 01701
e-mail: gtw5020@psu.edu

Timothy W. Simpson

Department of Mechanical Engineering,
The Pennsylvania State University,
State College, PA 16801
e-mail: tw8@psu.edu

Nicholas Meisel

School of Engineering Design and Innovation,
The Pennsylvania State University,
State College, PA 16801
e-mail: nam20@psu.edu

Sneha Prabha Narra

Department of Mechanical Engineering,
Carnegie Mellon University,
Pittsburgh, PA 15213
e-mail: snarra@andrew.cmu.edu

Christopher McComb¹

Department of Mechanical Engineering,
Carnegie Mellon University,
Pittsburgh, PA 15213
e-mail: ccm@cmu.edu

Accelerating Thermal Simulations in Additive Manufacturing by Training Physics-Informed Neural Networks With Randomly Synthesized Data

*The temperature history of an additively manufactured part plays a critical role in determining process–structure–property relationships in fusion-based additive manufacturing (AM) processes. Therefore, fast thermal simulation methods are needed for a variety of AM tasks, from temperature history prediction for part design and process planning to in situ temperature monitoring and control during manufacturing. However, conventional numerical simulation methods fall short in satisfying the strict requirements of time efficiency in these applications due to the large space and time scales of the required multiscale simulation. While data-driven surrogate models are of interest for their rapid computation capabilities, the performance of these models relies on the size and quality of the training data, which is often prohibitively expensive to create. **Physics-informed neural networks (PINNs) mitigate the need for large datasets by imposing physical principles during the training process. This work investigates the use of a PINN to predict the time-varying temperature distribution in a part during manufacturing with laser powder bed fusion (L-PBF). Notably, the use of the PINN in this study enables the model to be trained solely on randomly synthesized data. These training data are both inexpensive to obtain, and the presence of stochasticity in the dataset improves the generalizability of the trained model.** Results show that the PINN model achieves higher accuracy than a comparable artificial neural network trained on labeled data. Further, the PINN model trained in this work maintains high accuracy in predicting temperature for laser path scanning strategies unseen in the training data. [DOI: 10.1115/1.4062852]*

Keywords: computational foundations for additive manufacturing, computer aided manufacturing, machine learning for engineering applications

1 Introduction

Additive manufacturing (AM) processes have demonstrated the advantages of fabricating products with complex geometries, intricate cellular structures, and unique properties [1–4]. However, the quality of AM parts has proved difficult to control because of the unpredictable residual stress, defects, and other properties [5]. To make the metal AM process more predictable and controllable, researchers have extensively investigated process–structure–property relationships [6–11]. Especially in fusion-based metal AM processes, temperature history plays a crucial role in determining the part properties [12–15] as it affects important aspects of the AM

process, such as the melt pool dimensions [16], defect formation [17–19], solidification conditions, remelting cycles [20,21], and residual stress [22]. Therefore, accurate prediction and monitoring of temperature history during the AM process can aid in capturing the essential elements of the process–structure–property relationships. Since experiments are usually expensive, thermal simulations of AM processes is critical for the study of the process–structure–property relationships [12,23].

Although this work focuses on the laser powder bed fusion (L-PBF) AM process, the machine learning (ML) model and training strategies introduced here could apply to other fusion-based AM processes by changing the relevant physical principles and processing parameters. Simulating L-PBF thermal phenomena involves analyzing temperature changes at sub-nanosecond timescales [24], several orders of magnitude shorter than the entire build duration. As a result of the high temporal resolution requirements, full

¹Corresponding author.

Manuscript received February 1, 2023; final manuscript received June 16, 2023; published online July 20, 2023. Assoc. Editor: Anurag Purwar.

simulations of an L-PBF build can take several hours to days [14,25]. Accordingly, the time cost is prohibitively high for iterative optimization applications, such as those that are common in design for AM (DfAM) [25], process parameter planning [26], and in situ process monitoring and control [27,28].

To reduce the computational cost associated with simulation models in AM processing, some researchers have adopted surrogate modeling techniques that can yield results significantly faster than traditional physics-based simulations, as demonstrated in studies by Gu et al. [29], Wang and Behandish [30], and Stathatos and Vosniakos [31]. Artificial neural networks (ANNs) are a typical means of constructing surrogate models, as they can be trained to emulate existing simulation data. While there have been successes in implementing ANN surrogate models for AM that are faster than traditional numerical methods, the generation of high-quality training data still depends on computationally intensive physics-based simulations, as noted in several studies [31–33]. This bottleneck in generating training data has led to slow progress in developing and refining these models. Besides, the diverse geometries of the printed parts and the various process parameters of AM require enormous training data; otherwise, the trained models may lack generalizability and can be applied only in limited situations. Thus, overcoming this challenge would allow for more rapid iteration and improvement of ANN models in AM.

While numerical simulations can be prohibitively expensive, and ANNs require large amounts of data that can be equally costly, physics-informed neural networks (PINNs) represent a promising approach to significantly reducing the expense, as demonstrated in studies by Karniadakis et al. [34], Kats et al. [33], and Elhamod et al. [35]. PINNs achieve this by incorporating physical principles in the form of partial differential equations (PDEs), which enhances the physical accuracy of the solutions [36]. In addition, since the development time of L-PBF surrogate models is typically a key consideration, the optimal PINN architecture should be designed to use inexpensive training data, while still enabling generalizability, as noted by Shin et al. [37].

In this work, we introduce an ML method that employs inexpensive synthesized data to enable rapid transient thermal simulation during L-PBF. Our method predicts the temperature distribution over the voxelized space in the next time-step based on the current distribution. The synthesized data are procedurally generated as a set of temperature and heat generation fields in which each voxel was uniformly assigned a random value between a prescribed range. Importantly, the model is generalizable in an L-PBF transient thermal simulation application where the input temperature distributions are determined by scanning strategies unseen in the training data.

This work conducts numerical experiments to analyze the effects of PINN on the transient thermal simulations and test the performance of the PINN trained with synthesized data on the L-PBF simulations obtained by traditional numerical methods, treated as a ground truth. Therefore, the research questions for this article can be summarized as follows:

- (1) How does a PINN compare to a traditional label-trained ANN over an extensive range of randomly synthesized data in terms of aggregate prediction error?
- (2) How does a PINN compare, in terms of prediction error over time, to a traditional label-trained ANN based on a ground truth model in L-PBF thermal analysis problems?

As this article aims to report the emerging ML techniques that can be applied to fast AM thermal simulation, we do not implement the most advanced physics simulations to generate the training data but work with a finite difference (FD) method for transient heat conduction without considering the nonlinearities introduced by phase transitions and temperature-dependent properties. Although simplified, the ML model can capture the patterns contained in the numerical method.

The remainder of this article is organized as follows. Section 2 provides relevant background information on L-PBF simulation,

ML methods applied to L-PBF, and physics-informed ML. Section 3 introduces the experimental methods, including the ground truth model, ANN architecture, and numerical experimental design. Section 4 communicates the results of the numerical experiments, and Sec. 5 summarizes key results and identifies avenues for future work.

2 Background

This section provides relevant background information on ML and ANN methods in L-PBF (see Sec. 2.1) and related work involving PINNs (see Sec. 2.2).

2.1 Machine Learning for L-PBF. There is an abundance of ML applications in various domains of L-PBF [38]. For example, in DfAM, generative ML models are trained to optimize cellular structures and topologies [39–41]. In manufacturing, ML can be used for manufacturability analysis [42], pre-manufacturing planning [43,44], and product quality assessment and control [45,46]. In this article, the scope is under the topic of applying ML for process monitoring. The L-PBF process is highly dependent on conditions within the manufacturing environment, so gathering and processing data while L-PBF builds are ongoing is a lucrative way of preventing failures or optimizing the process parameters. ML approaches can analyze the images of the melt pool to make predictions about the properties of the melt pool and defects [47,48]. However, potentially large amounts of data are usually needed to train the ML models for monitoring and making in situ adjustments to the L-PBF process. For example, Kwon et al. reported several hundred gigabytes of image data for one build [48]. Yang et al. [47] collected 118,928 images of melt pools after only 21 layers of an L-PBF build. While it is difficult to assign labels to such many images, an advantageous alternative is applying domain knowledge to this problem. Besides, Bugatti and Colosimo put forward a small data extraction method that only extracts the relevant information from high-speed imaging data for in situ monitoring of hot-spot defects in L-PBF [49]. Ren and Wang incorporated physics-informed input features in addition to the melt pool images to help the training process [50]. ML methods have also been used for simulation purposes to predict the outcome of the L-PBF process; however, this method typically utilizes commercial simulation software to generate validation data [51]. In addition to the applications mentioned, an important concept to consider in L-PBF models is the ability to form hybrid models. Moges et al. demonstrated the success of a hybrid model involving the combination of traditional numerical analysis and ML/ANN-based surrogate models for melt pool prediction with improved accuracy and without the loss of speed [52]. Instead of analyzing the images directly, Smoqi et al. depended on the physics-informed melt pool signatures from an in situ dual-wavelength imaging pyrometer to monitor and predict porosity in L-PBF. [53]. Similarly, Vela et al. put forward an ML approach that can evaluate the intrinsic resistance to balling of alloys based on the intrinsic thermophysical properties for design alloys [54]. Notably, few-shot learning (FSL) is a novel machine learning algorithm that has been developed to train ML models on small datasets using prior knowledge to augment the data, reduce the hypothesis space, or guide the search to minimize the loss function [55]. However, FSL requires prior knowledge gained from a large base dataset, which makes it unsuitable for application in AM simulation at the current stage, as such a dataset has not yet been created. Nevertheless, FSL has the potential to enable ML models to generalize to unique geometries in the future.

2.2 Related Work in Physics-Informed Neural Networks. PINNs refer to any deep learning technique that encodes knowledge of a PDE into the network itself to solve the PDE. As a result, a variety of attempts have been made to apply this approach to

solve PDEs and engineering problems that involve PDEs. The article by Shin et al. [37] provides a comprehensive review of these efforts and their convergence properties. Raissi et al. introduced a framework for using PINNs to solve nonlinear PDEs for continuous and discrete-time modes [56]. In the field of AM, PINNs have been employed for thermal simulation. Zhu et al. [32] proposed a PINN framework based on fully connected neural networks, which incorporates the conservation laws of momentum, mass, and energy into the learning process. Moreover, they developed a hard-type approach for Dirichlet boundary conditions utilizing a Heaviside function. Liao et al. [57] proposed a hybrid thermal prediction framework that integrates partially observed temperature data with physics laws to predict the complete temperature history and determine material and process parameters.

Studies have demonstrated that PINNs can achieve consistent convergence to the accurate PDE solution, even when the training dataset is corrupted with noise. This finding suggests that an accurate model can still be developed with data that does not appear experimentally. Silvestri et al. [58] discuss this phenomenon and the effectiveness of injecting noise into the training process to improve the robustness of the model. This PINN framework by Raissi et al. also introduced the idea of using automatic differentiation of backpropagation instead of numerical differentiation for penalizing the physics-informed loss. The current work uses FD to calculate the residual of the PDEs, but the method of automatic differentiation is common in most recent PINN research, with novel applications to Navier–Stokes equations, subsurface flow, noisy forward and inverse problems, time-dependent PDEs, and performance iterations on the linear PDE PINN architecture [59–63]. In general, the architectures and training data used with PINNs are quite varied, each tailored to the specific problem being investigated. One notable example that is particularly relevant to the current work is from Wang et al., who developed a nonautomatic differentiation, finite time difference, and PINN for transient electromagnetic analysis using a recurrent neural network [64]. Training data were created by randomly generating wave point sources and interference objects. The goal of this method was to quickly simulate abstract scenarios without numerical methods, taking advantage of one of the main benefits of the PINN method toward inexpensive training. It is distinct from some of the automatic differentiation approaches that only lightly apply noise to training data instead of fully abstract data. Liu and Wang created a physics constrained neural network (PCNN) for the 2D heat equation [65]. The PCNN method is similar to the PINN method in that it encodes physics domain knowledge; however, it still uses labeled training data in tandem with the physics-based loss function. The goal of this method is to reduce the amount of labeled data required and to also enforce the physical constraint. For our work, the success of the heat equation PCNN is of particular interest for L-PBF simulation as discussed next.

3 Proposed Methods and Assumptions

This section details the methods and assumptions regarding the L-PBF FD method used here as a ground truth model (see Sec. 3.1), the layer architecture shared by the PINN, and the label-trained ANN (see Sec. 3.2), the L-PBF numerical experimental design (see Sec. 3.3), and the experimental approach used to compare the PINN and label-trained ANN (see Sec. 3.4). All methods are of numerical study; no comparison is made with experimental data in the current work.

3.1 Finite Difference Method for L-PBF Ground Truth.

The current work uses a 3D FD method tailored for AM proposed by Stockman et al. [66]. This model analyzes the transient temperature of a volume of fused powder in a laser direct energy deposition (DED) machine and includes conduction, convective boundary, and Dirichlet boundary conditions. DED is similar to L-PBF in that it often uses a laser to fuse powdered metal into a

specific shape; however, it does not use a large bed of powder. To accurately represent the L-PBF process instead of DED, internal heat generation (energy transfer) was added in place of the constant temperature Dirichlet boundary condition used to approximate the laser source. Approximating the laser source as internal heat generation is a common assumption used in L-PBF simulation [67,68]. There are many approaches to modeling this internal heat generation, but for our approach, one voxel was heated at a time [69]. The radiative boundary was not included. The transient heat transfer PDEs are provided in Eq. (1).

$$\begin{aligned} \rho c \frac{\partial T}{\partial t} - \nabla \cdot (k_p \nabla T) - s &= 0 \\ (1) \text{ Dirichlet } T &= T_1(x, y, z) \text{ on } \Gamma_1 \\ (2) \text{ Neumann } q &= -q_s \text{ on } \Gamma_2 \\ (3) \text{ Neumann } q &= -h_c(T - T_{\text{amb}}) \text{ on } \Gamma_3 \end{aligned} \quad (1)$$

where ρ is the material density, c is the specific heat capacity, T is the temperature, t is time, k_p is the material conductivity, s is the heat generate rate per unit volume, q_s is the external heat flux, h_c is the convection coefficient, T_{amb} is the ambient temperature, and Γ_1 , Γ_2 , and Γ_3 are the surfaces where each boundary condition is applied on.

The numerical method is formulated as follows. For voxels that only pertain to conduction and Dirichlet boundary conditions, indicated in Fig. 1, the equation is

$$\begin{aligned} T_{i,j,k}^{n+1} &= \text{Fo}(T_{i+1,j,k}^n + T_{i-1,j,k}^n + T_{i,j+1,k}^n + T_{i,j-1,k}^n \\ &\quad + T_{i,j,k+1}^n + T_{i,j,k-1}^n + \frac{Q_{i,j,k}^n}{k_p} - 6T_{i,j,k}^n) + T_{i,j,k}^n \end{aligned} \quad (2)$$

where $T_{i,j,k}^n$ is the absolute temperature at the current time-step n of a node at positions i, j, k (corresponding to the x, y, z coordinates), $T_{i,j,k}^{n+1}$ is the absolute temperature at the future $n+1$ time-step, $Q_{i,j,k}^n$ is the current time-step n heat generated at node i, j, k , and Fo is the Fourier number found in Eq. (3):

$$\text{Fo} = \frac{k_p dt}{h^2 \rho c} \quad (3)$$

where k_p is the thermal conductivity of the powder, dt is the time-step, h is the cubic voxel side length, ρ is the density of the powder, and c is the specific heat of the powder. For voxels that involve conduction and convection, indicated in Fig. 1, the

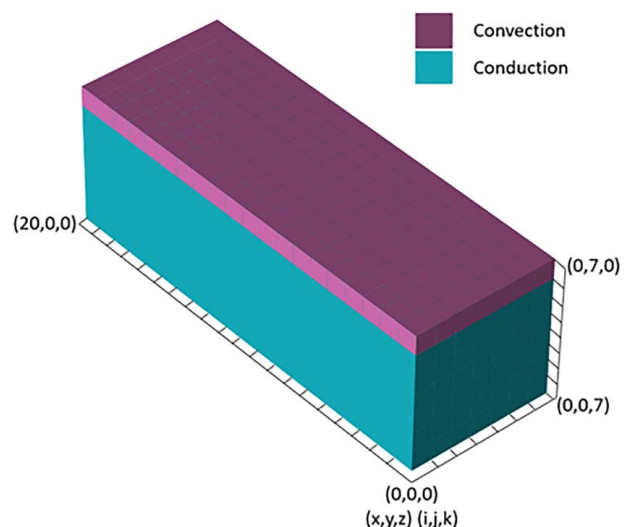


Fig. 1 Visualization of boundary condition locations used with the finite difference equations (2) and (4)

equation is modified as follows:

$$T_{i,j,k}^{n+1} = \text{Fo}(2\text{Bi}T_{i,j-1,k}^n + 2T_{i,j+1,k}^n + T_{i,j,k+1}^n + T_{i,j,k-1}^n + T_{i,j,k}^n(-2\text{Bi}-6)) + T_{i,j,k}^n + \frac{Q_{i,j,k}^n}{k_p} + T_{i,j,k}^n \quad (4)$$

where Bi is the Biot number, which is computed as follows:

$$\text{Bi} = \frac{Ch}{k_a} \quad (5)$$

where C is the heat transfer coefficient of air and k_a is the thermal conductivity of air.

By using the FD method in conjunction with voxel representation, the equation that calculates temperature at each voxel can be generalized for every volumetric region of interest in the powder volume to a desired resolution. Equation (2) applies to all interior voxels connected to the conduction voxels seen in Fig. 1 and all other interior voxels not connected to a boundary condition. Meanwhile, Eq. (4) applies to all interior voxels connected to convection voxels (see Fig. 1).

3.2 Artificial Neural Network Architecture Design. In order to facilitate comparison between the PINN and a label-trained ANN, the training parameters, training data, and physical constants of the PINN and the label-trained ANN were held constant. This section details the shared ANN architecture of the PINN and the label-trained ANN (see Sec. 3.2.1), the custom loss function of the PINN (see Sec. 3.2.2), and the design of the shared training dataset (see Sec. 3.2.3).

3.2.1 PINN and Label-Trained Artificial Neural Network Architecture. The simulated volume used as the input for the PINN and the label-trained ANN had a voxel dimension of $20 \times 7 \times 7$. Each voxel is encoded a two-channel vector representing the temperature and heat generation magnitude at each voxel at a particular instant in time, making the total input size $20 \times 7 \times 7 \times 2 = 1960$. The output of the PINN and the label-trained ANN is a $20 \times 7 \times 7 = 980$ voxel-based field, where each voxel represents the estimated temperature of the region after one additional time-step has passed. Both of these models are discrete-time models, where input data describing the temperature and heat transfer field are used to predict a temperature field at a fixed time-step. The loss function of the PINN only iterates through the interior nodes of the input since the outer layers of the input space are encoded as the boundary conditions for the temperature channel (see Fig. 1) or exist as “padding” for the heat generation channel. In order to match the dimensionality of the input, the outer voxels of the output also serve as padding. Since the L-PBF application requires predicting an entire scalar field throughout a volume, it necessitates a model with a relatively high output dimensionality. Therefore, a convolutional neural network (CNN) architecture was selected because CNNs are particularly advantageous at retaining practicable training times with increases in input and output dimensionality [70]. The shared architecture of both the PINN and label-trained ANN is specified in Fig. 2 for our work.

The shared architecture in Fig. 2 is developed in TENSORFLOW version 2.1.0, KERAS version 2.3.1, and PYTHON version 3.7.6. The ANNs were trained using a GTX 1080 Ti GPU, while the FD was executed using an Intel 4770 K CPU. The PINN and the label-trained ANN were trained using the same 5000 training samples with a batch size of 100 samples for 50 epochs, which we selected qualitatively as values at which training/testing loss has converged for all models. The Adam optimizer was used with a learning rate of 5×10^{-4} . The label-trained ANN used mean squared error (MSE) as the loss function, while the PINN used the loss function described in the next section.

3.2.2 PINN Loss Function. The PINN custom loss function for this case is constructed as the MSE of the conduction and

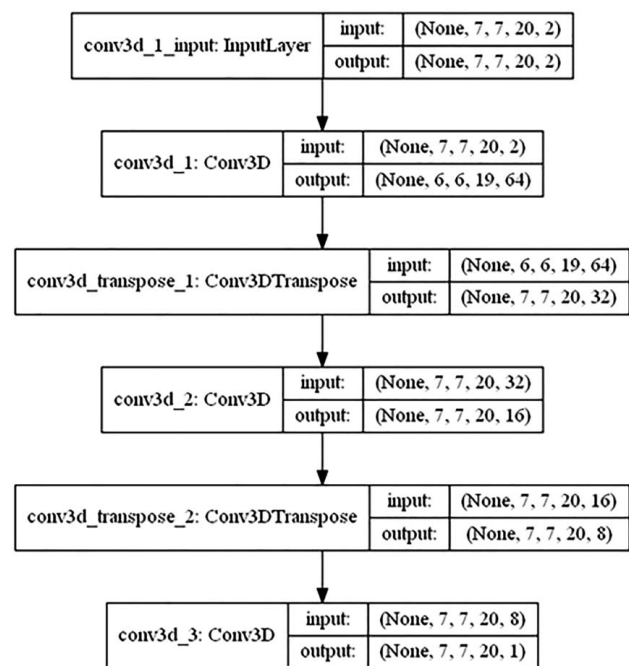


Fig. 2 Flowchart of shared PINN and label-trained ANN architecture layers

convection finite difference equations. Since loss should approach zero during training, the future time-step solution is subtracted from the current temperature added with the temperature change calculated by FD. The loss equation corresponding to voxels with only conduction and heat generation is given by

$$\text{Loss}_a = \sum_{i=1}^7 \sum_{j=1}^7 \sum_{k=1}^{20} |T_{i,j,k}^n + (\Delta T_{i,j,k}^n)_{\text{cond}} - T_{i,j,k}^{n+1}| \quad (6)$$

where $T_{i,j,k}^n$ is the current n time-step temperature of the voxel at position i, j, k (indices corresponding to the x, y , and z axes, respectively), $(\Delta T_{i,j,k}^n)_{\text{cond}}$ is the change in temperature calculated using Eq. (2), and $T_{i,j,k}^{n+1}$ is the future $n+1$ temperature predicted by the PINN. The loss equation corresponding to voxels with conduction, convection, and heat generation is computed as follows:

$$\text{Loss}_b = \sum_{i=1}^7 \sum_{j=1}^7 \sum_{k=1}^{20} |T_{i,j,k}^n + (\Delta T_{i,j,k}^n)_{\text{conv}} - T_{i,j,k}^{n+1}| \quad (7)$$

where $(\Delta T_{i,j,k}^n)_{\text{conv}}$ is the change in temperature calculated using Eq. (4), and $T_{i,j,k}^{n+1}$ is the future $n+1$ temperature predicted by the PINN. The loss equations are then combined using

$$\text{Loss} = \frac{(\text{Loss}_a + \text{Loss}_b)^2}{N} \quad (8)$$

where N is the number of voxels included in the loss calculation (here, $N=450$ based on the discretization). All loss calculations are also normalized for the size of the datasets used.

3.2.3 Training Dataset Design. To eliminate the need for prohibitively expensive labeled data, synthesized data can be advantageous. Existing PINN methods incorporate many different approaches for generating training data without relying on costly or unavailable experimental observations. For instance, one approach used experimental data with 1% noise [58]. A second approach randomly generated shapes in order to mimic experimental training data [64]. An important goal of this work is to maximize the speed of generating training data while minimizing the potential bias toward a small number of researcher-selected conditions. To

achieve this goal, we procedurally generated a set of temperature and heat generation fields in which each voxel was uniformly assigned a random value between -100 and 100 (for both temperature, measured in Kelvin, and energy transfer, measured in Watts). This range was intentionally below the order of magnitude of temperatures and approximately on the order of magnitude for heat generation values experienced in a powder bed volume after melt pool solidification in order to keep the input data uniform and simple. Here, positive values represent heat generation within a voxel, and negative values represent heat absorption. For temperature, although half of the data is below 0 K, the loss function used is continuous for all temperature values. **In other application areas, the selection of the range for the random values should be treated as an additional hyperparameter in the end-to-end PINN training process. An example of a training data sample (for the temperature or heat transfer channel) can be seen in Fig. 3.**

In addition to the training data, the training process is constrained globally with temperature boundary conditions that hold constant at a value of 293 K. The cubic voxel side length was 1×10^{-7} m with a constant time-step length of 2.7×10^{-8} s. This voxel size is below the typical size for the powdered metal in L-PBF, which allows this model to better simulate an effective homogeneous medium [71]. The material properties chosen were as follows: 0.1 W/m·K for the powder thermal conductivity, 0.02 W/m·K for the air thermal conductivity, 25 W/m²·K for the heat transfer coefficient, 8000 kg/m³ for the powder density, and 420 J/K·kg for the specific heat [71–74]. These values are within the range of numbers found in metal L-PBF processes. An important constant to mention is the thermal conductivity of the powder. While metal powders typically used in L-PBF have conductivities of 10 – 200 W/m·K, research shows that due to the packing density and composition of the air, the effective value is much lower [74].

3.3 L-PBF Application Problem Statement. Transient thermal analyses of an L-PBF process assessed the performance of the PINN. As previously mentioned, the FD method used for the loss function is already tailored for AM [66], with some modifications as noted in Sec. 3.1. Heat conduction is modeled with Dirichlet boundary conditions on five exterior faces of the temperature field and a convection boundary condition on the top surface. The laser is modeled using a single internal heat source approach, where 1 voxel is heated at a time. The boundary conditions on all six faces are constrained by a temperature value of 293 K. The first simulation involves two sequential modes: (1) a single laser track and (2) a diffusion mode with no heat generation. From $t = 0$ – 504 ns (where $t = 0$ is defined as the first prediction), a 1000 -watt heat source moves voxel-by-voxel along the top plane of the temperature field. This approximates a laser moving at

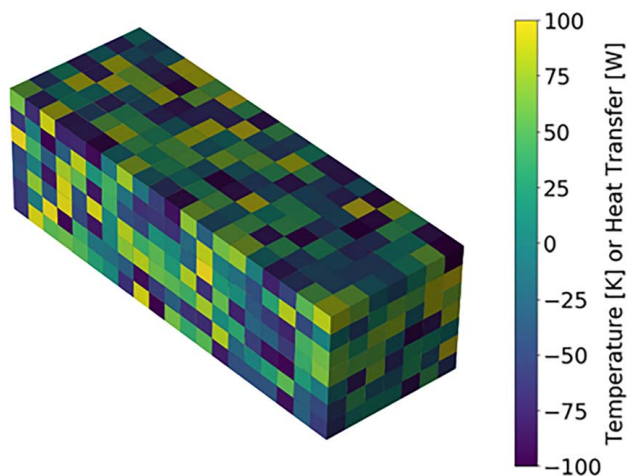


Fig. 3 Example 3D plot of uniformly randomly generated temperature channel and heat transfer channel training data

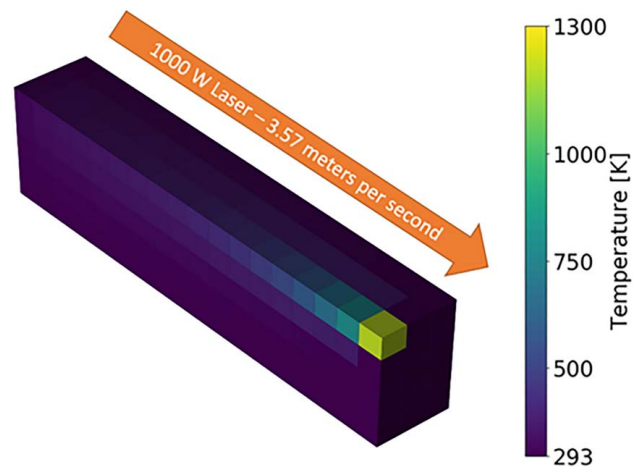


Fig. 4 Visualization showing cutaway view of the ground truth temperature through the powder bed volume after 504 ns of laser radiation

3.57 m/s. These numbers are within the range of values found in L-PBF processes [75,76]. After the $t = 504$ ns, the heat source is turned off, and the temperature field approaches a steady state until $t = 2772$ ns is reached. A cutaway of the FD simulation result at $t = 504$ ns is shown in Fig. 4.

We then formulated three different scan patterns as shown in Fig. 5. These scan patterns each use a different laser scanning strategy in order to assess the versatility of PINNs and label-trained ANNs over different scan pattern types. Each scan pattern takes 1400 ns to complete and is repeated ten times for a total simulation length of $14,000$ ns. This repetition enables an assessment of error accumulation achieved by both the PINN or label-trained ANN compared to the ground truth model.

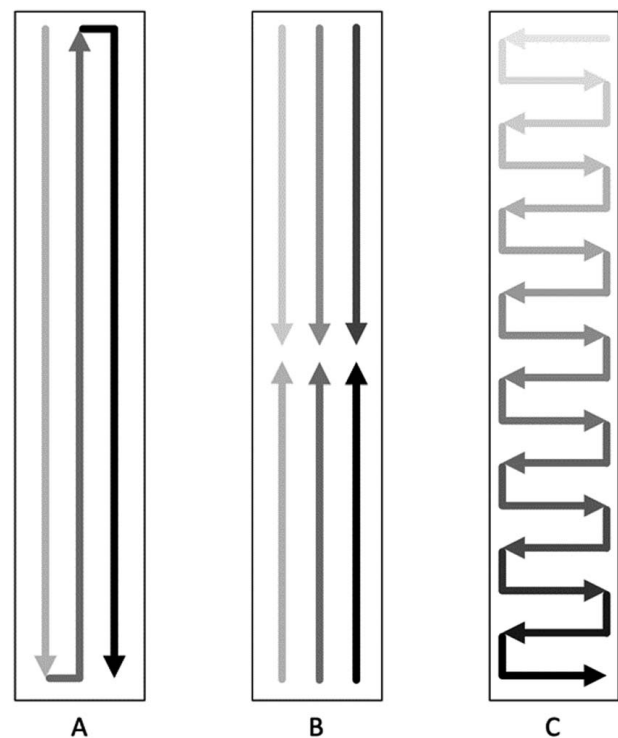


Fig. 5 Top-down view of different scanning strategies used to demonstrate surrogate models. Lighter shades represent the beginning of a scan pattern, and shades darken as the scan progresses.

3.4 Numerical Experimental Design. To investigate differences in the PINN training method and the label-trained method, we compared the aggregate prediction error of 30 pairs of the PINN and label-trained ANN in a one-sided Wilcoxon signed-rank test [77,78]. Each pair of PINN and label-trained ANN models was trained with the parameters found in Sec. 3.2.3 with a different random number seed for each pair. Each pair of PINN and label-trained ANN models was also tested on a dataset generated similarly to the training dataset. However, instead of values between -100 and 100 , we selected 1000 samples of a much larger range of $100-10,000$ K in order to test unseen data out of the training range and evaluate the generalizability of the model. Each pair also used a shared seed for a total of 30 training datasets, 30 testing datasets, and 30 different seed pairs. Each sample is only fed through the network once; so, this does not evaluate compounding error. We tested each PINN and label-trained ANN model by directly comparing the predictions to the FD ground truth (ground truth minus prediction) and calculating the mean of these prediction errors per model. These means were then compared using a Wilcoxon signed-rank test [79] in order to demonstrate the difference between the two different training methods aggregate error biases. In order to compare the distribution of prediction error between the two models, the mean standard deviation of the 30 pairs was also calculated. The FD L-PBF simulations serve as the ground truth model for the PINN method since the PINN loss function is derived from the same FD equations. For demonstrative purposes, we selected the two best PINN and label-trained ANN models from the 30 models tested in the Wilcoxon signed-rank test (based on mean prediction error). The first FD L-PBF simulation (with two simulation modes) is compared to the ANNs in two ways: (1) mean absolute percent error (MAPE) over time and (2) a visual inspection of error per voxel over time. MAPE was chosen as a way of continuously evaluating the aggregate temperature field error of each time-step. By evaluating this metric over time, we can learn how each ANN performs in each simulation mode defined in Sec. 3.3. By calculating and displaying the error for each voxel over time, it is also possible to empirically evaluate the source of error for each ANN. The three different scanning patterns are compared using MAPE over time.

4 Results

This section presents the results of the Wilcoxon signed-rank tests (see Sec. 4.1) and L-PBF simulations (see Sec. 4.2). These results test our two research questions from Sec. 1.

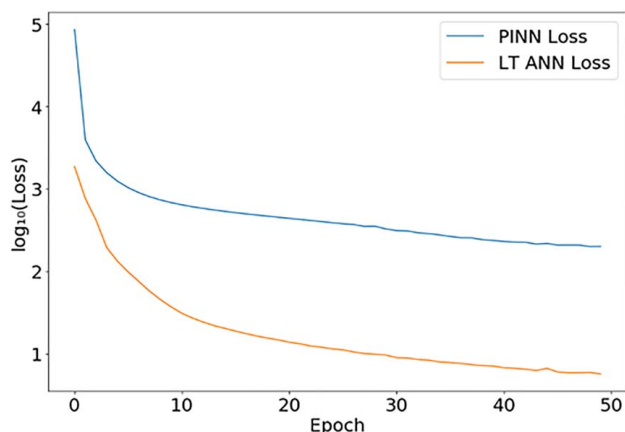


Fig. 6 Plot of example loss per epoch convergence for PINN and label-trained ANN models. Note that this picture does not mean to compare the performance of the two models as the terms in their loss functions are different.

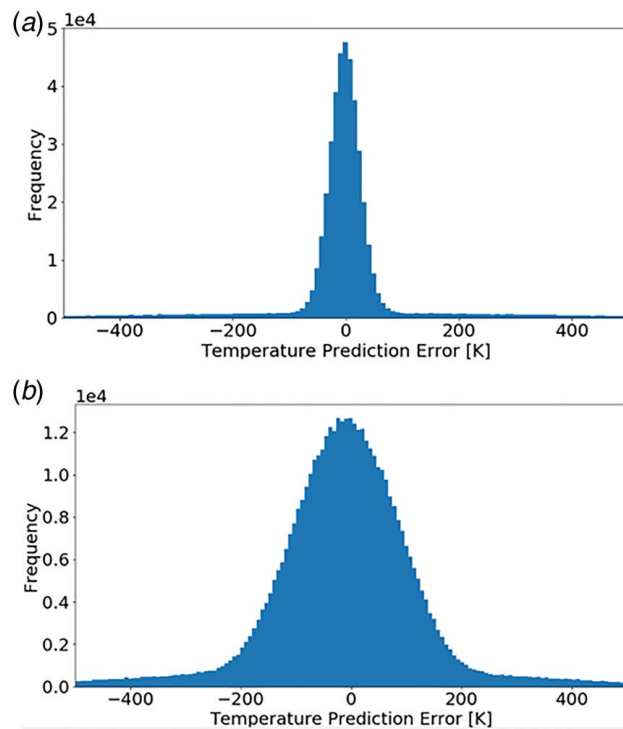


Fig. 7 Example histograms of the two best (a) PINN and (b) label-trained ANN predicted temperatures versus the FD ground truth temperature error residuals

4.1 Comparison of PINN and Label-Trained Artificial Neural Networks. For the first research question, we assess how PINN models compare to label-trained ANN models over an extensive range of randomly synthesized data. The training results of one sample of seed paired PINN and label-trained ANN models are shown in Fig. 6. Both training methods converged similarly, with different loss values due to the different loss functions used.

The Wilcoxon signed-rank test dataset was calculated for the aggregate prediction error of 30 pairs of PINN and label-trained models. This test gave a p -value of 14.5%, showing the significance that the PINN has a different aggregate prediction bias compared to the label-trained ANN. In addition to the statistical test, we also show the distribution of predictions from the two best models (based on mean bias) in Fig. 7.

Although in general the PINN predictions appear to have a smaller standard deviation, the actual mean standard deviation across all 30 pairs is 150.0 for the PINN and 149.8 for the label-trained ANN. Because the standard deviations are relatively

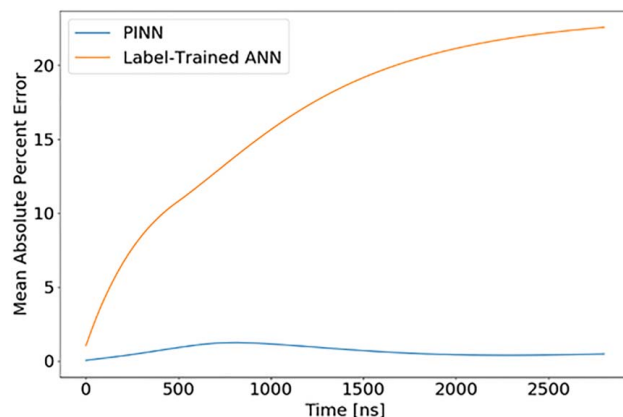


Fig. 8 Plot of MAPE versus time for the PINN and label-trained ANN L-PBF 2 mode simulation

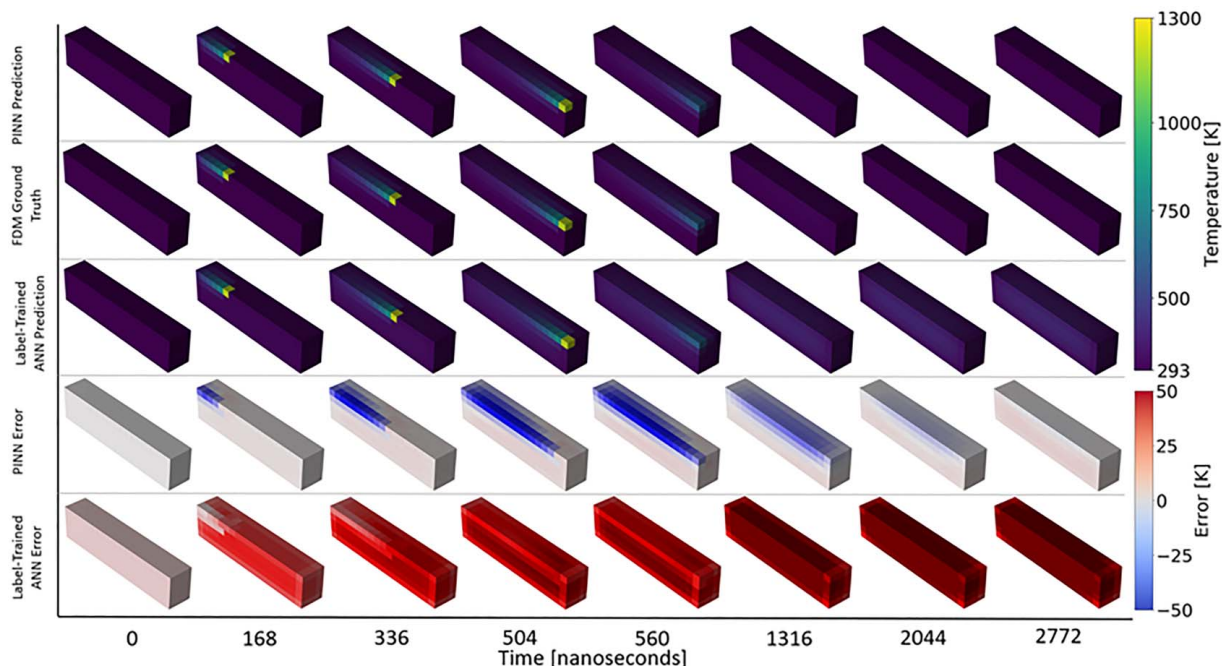


Fig. 9 Cutaway plots of PINN simulation, FD ground truth simulation, label-trained ANN simulation, PINN error, and label-trained ANN error at selected time-steps

similar, the absolute value of the aggregate prediction bias acts as a better indicator of model performance.

4.2 L-PBF Inspired Simulation. For the second research question, we assess how the PINN performs over time in a L-PBF simulation compared to the label-trained ANN. The L-PBF simulation involves compounding time-steps and as a result produces more divergent results between the PINN and label-trained ANN than the previous section, even though both models selected had relatively low mean biases. For the PINN, MAPE peaked at a value of 1.24%, while the label-trained ANN peaked at a value of 22.5%. In the laser track simulation mode, both models increased error over time. In the conduction simulation mode, the PINN system approaches zero while the label-trained ANN does not. These results can be found in Fig. 8.

To visualize the transient simulation process across space as well as time, eight timestamps of the L-PBF simulation are shown for comparison in Fig. 9. The first four instances ($t = [0, 504]$ ns) demonstrate the laser track motion; the last four instances ($t = [504, 2772]$ ns) demonstrate the diffusion mode with no heat generation. In the first three rows, the authors plot the PINN, FD ground truth, and label-trained ANN simulations at the chosen time-steps. In the last two rows, the authors plot the error of the PINN and label-trained ANN predictions versus the ground truth FD model.

Visually, the simulations using both PINN and label-trained ANN appear very similar to the FD ground truth; however, the pattern of the error accumulation is not the same for the PINN and label-trained ANN. For the first four timestamps shown in Fig. 9, the PINN error mirrors the laser track. In the last four timestamps (after the laser is deactivated, and thermal activity enters a diffusion mode), the error is more symmetric throughout the temperature field and decreases over time. The label-trained ANN does not exhibit the same pattern of error as the PINN; it is more symmetric for all eight timestamps. Specifically, the error is concentrated toward the center of the temperature field rather than the boundary. The error for the label-trained ANN also increases over time. This demonstrates that the PINN architecture used in this work provides some degree of error-correcting capability during thermal diffusion.

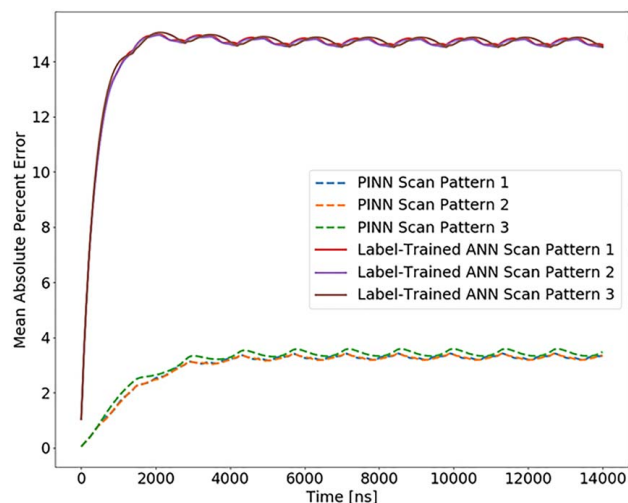


Fig. 10 Plot of the three different scan pattern simulation results for the PINN and label-trained ANNs

The results of the scanning pattern comparison are shown in Fig. 10. In contrast to the previous simulation, these simulations provide continuous laser activity. Little variation is observed between scan pattern types, indicating that both label-trained ANN and PINN results are robust across laser scan patterns. Specifically, we noted that the mean error of scan pattern 3 is slightly larger than that of the other patterns for the PINN model. **We attribute this difference to the fact that scan pattern 3 changes direction more frequently than the other patterns, which suggests that the synthesized data may capture fewer direction-changing features.** Moreover, both models reach a maximum error value during each scanning pattern. For the PINN model, the average maximum MAPE was 3.57%, while the label-trained model reached a maximum average value of 15.1%. In general, all scan patterns had roughly the same error pattern for the PINN and label-trained models. After an initial ramp-up period, the error pattern shows cyclicity that aligns with the repetition of the scan pattern.

5 Conclusions

For L-PBF, computational simulations are becoming increasingly crucial in optimizing the fabrication process and preventing failure. ML has become a powerful tool for making simulations such as these more rapid and accurate. This work specifically aimed to evaluate a method for eliminating the prohibitively expensive data labeling process and to train surrogate models using well-understood physics domain knowledge. Our work created an L-PBF heat transfer simulation that utilized a PINN with multiple boundary conditions trained on randomly synthesized data.

For the first research question, the authors investigated the statistical difference between our proposed PINN and a traditionally label-trained ANN. Our Wilcoxon signed-rank test demonstrated that, in general, it is likely that the PINN performs better than the label-trained ANN given the same training data and constraints. However, although the distribution of prediction errors appeared to be superior for the PINN, the standard deviations of both the PINN and label-trained ANNs prediction errors were the same. Knowing this, at a very minimum, the PINN performs equally to the label-trained ANN.

The second research question involved simulating L-PBF thermal problems. For these problems, the error was compounded over time, which further demonstrated the difference between the PINN and label-trained models. Upon comparing the two best models from the statistical test dataset, the PINN showed better MAPE over time in all simulation scenarios. Furthermore, upon visual analysis of the errors for each voxel, it was clear that the error pattern was different for the PINN compared to the label-trained ANN.

Our experiments showed that the randomness of the training data allows the ML model to maintain good accuracy even on well-organized scan patterns. However, there is still a long way to go from current research to practical implementation, as the current resolution and geometry are limited. **While the randomized synthesized data may not fully cover the range of possible scan patterns and geometries in real-world scenarios, it can still serve as a useful data augmentation method to improve the generalizability of the ML model when training data are limited.**

Although our proposed PINN showed promise compared to the traditionally label-trained ANN, especially in the L-PBF simulation, this work only involved a single PDE—the heat equation. This work also used many physical constants, many of which can change over time in a L-PBF build. Future work should extend this work by investigating the ability of stochastically trained PINNs to learn a wider variety of physical phenomena as well as investigating the robustness of the approach with respect to varying physical constants. Grounding the simulations in this work with respect to experimental data is also an important avenue of future work. **In addition, there are growing opportunities to embrace emerging ML methods to improve the current approach. This may include the use of new techniques for improving execution time (such as auto-differentiation) and the integration of new domain representations (such as graph neural networks).**

Acknowledgment

This material is based upon work supported by the National Science Foundation through Grant No. CMMI-1825535 and by Carnegie Mellon University's Manufacturing Futures Institute through the MFI Postdoctoral Fellowship Program. Any opinions, findings, conclusions, or recommendations expressed in this paper are those of the authors and do not necessarily reflect the views of the sponsors. An earlier version of this article was presented at the 2021 ASME IDETC Design Automation Conference [80].

Conflict of Interest

There are no conflicts of interest.

Data Availability Statement

The datasets generated and supporting the findings of this article are obtainable from the corresponding author upon reasonable request.

References

- [1] Blakey-Milner, B., Gradl, P., Snedden, G., Brooks, M., Pitot, J., Lopez, E., Leary, M., and Berto, F., 2021, "Metal Additive Manufacturing in Aerospace: A Review," *Mater. Des.*, **209**, p. 110008.
- [2] Loh, G. H., Pei, E., Harrison, D., and Monzón, M. D., 2018, "An Overview of Functionally Graded Additive Manufacturing," *Addit. Manuf.*, **23**, pp. 34–44.
- [3] Nazir, A., Abate, K. M., Kumar, A., and Jeng, J.-Y., 2019, "A State-of-the-Art Review on Types, Design, Optimization, and Additive Manufacturing of Cellular Structures," *Int. J. Adv. Manuf. Technol.*, **104**(9), pp. 3489–3510.
- [4] Narra, S. P., 2022, "Powder Bed Fusion—Metals," *Encyclopedia of Materials: Metals and Alloys*, **3**(1), pp. 85–94.
- [5] Wang, C., Tan, X., Tor, S., and Lim, C., 2020, "Machine Learning in Additive Manufacturing: State-of-the-Art and Perspectives," *Addit. Manuf.*, **36**, p. 101538.
- [6] Kouraytem, N., Li, X., Tan, W., Kappes, B., and Spear, A. D., 2021, "Modeling Process–Structure–Property Relationships in Metal Additive Manufacturing: A Review on Physics-Driven Versus Data-Driven Approaches," *J. Phys.: Mater.*, **4**(3), p. 032002.
- [7] Luo, Q., Yin, L., Simpson, T. W., and Beese, A. M., 2023, "Dataset of Process-Structure-Property Feature Relationship for Laser Powder Bed Fusion Additive Manufactured Ti-6Al-4V Material," *Data in Brief*, **46**, p. 108911.
- [8] Popova, E., Rodgers, T. M., Gong, X., Cecen, A., Madison, J. D., and Kalidindi, S. R., 2017, "Process-Structure Linkages Using a Data Science Approach: Application to Simulated Additive Manufacturing Data," *Int. Mater. Manuf. Innovat.*, **6**(1), pp. 54–68.
- [9] Gordon, J. V., Narra, S. P., Cunningham, R. W., Liu, H., Chen, H., Suter, R. M., Beuth, J. L., and Rollett, A. D., 2020, "Defect Structure Process Maps for Laser Powder Bed Fusion Additive Manufacturing," *Addit. Manuf.*, **36**, p. 101552.
- [10] Fang, L., Cheng, L., Glerum, J. A., Bennett, J., Cao, J., and Wagner, G. J., 2022, "Data-Driven Analysis of Process, Structure, and Properties of Additively Manufactured Inconel 718 Thin Walls," *npj Comput. Mater.*, **8**(1), pp. 1–15.
- [11] Thanki, A., Goossens, L., Ompusunggu, A. P., Bayat, M., Bey-Temsamani, A., Van Hooreweder, B., Kruth, J.-P., and Witvrouw, A., 2022, "Melt Pool Feature Analysis Using a High-Speed Coaxial Monitoring System for Laser Powder Bed Fusion of Ti-6Al-4 V Grade 23," *Int. J. Adv. Manuf. Technol.*, **120**(9), pp. 6497–6514.
- [12] Nijhuis, B., and Geijselaers, H., 2021, "Efficient Thermal Simulation of Large-Scale Metal Additive Manufacturing Using Hot Element Addition," *Comput. Struct.*, **245**, p. 106463.
- [13] Ding, D., Zhang, S., Lu, Q., Pan, Z., Li, H., and Wang, K., 2021, "The Well-Distributed Volumetric Heat Source Model for Numerical Simulation of Wire Arc Additive Manufacturing Process," *Mater. Today Communicat.*, **27**, p. 102430.
- [14] Ness, K. L., Paul, A., Sun, L., and Zhang, Z., 2022, "Towards a Generic Physics-Based Machine Learning Model for Geometry Invariant Thermal History Prediction in Additive Manufacturing," *J. Mater. Process. Technol.*, **302**, p. 117472.
- [15] Dong, W., Jimenez, X. A., and To, A. C., 2023, "Temperature-Dependent Modified Inherent Strain Method for Predicting Residual Stress and Distortion of Ti6Al-4V Walls Manufactured by Wire-Arc Directed Energy Deposition," *Addit. Manuf.*, **62**, p. 103386.
- [16] Cook, P. S., and Murphy, A. B., 2020, "Simulation of Melt Pool Behaviour During Additive Manufacturing: Underlying Physics and Progress," *Addit. Manuf.*, **31**, p. 100909.
- [17] Wang, L., Zhang, Y., and Yan, W., 2020, "Evaporation Model for Keyhole Dynamics During Additive Manufacturing of Metal," *Phys. Rev. Appl.*, **14**(6), p. 064039.
- [18] Kiss, A. M., Fong, A. Y., Calt, N. P., Thampy, V., Martin, A. A., Depond, P. J., Wang, J., et al., 2019, "Laser-Induced Keyhole Defect Dynamics During Metal Additive Manufacturing," *Adv. Eng. Mater.*, **21**(10), p. 1900455.
- [19] Mukherjee, T., and DebRoy, T., 2018, "Mitigation of Lack of Fusion Defects in Powder Bed Fusion Additive Manufacturing," *J. Manuf. Processes*, **36**, pp. 442–449.
- [20] Vastola, G., Zhang, G., Pei, Q., and Zhang, Y.-W., 2015, "Modeling and Control of Remelting in High-Energy Beam Additive Manufacturing," *Addit. Manuf.*, **7**, pp. 57–63.
- [21] Zhu, Y.-Y., Tang, H.-B., Li, Z., Xu, C., and He, B., 2019, "Solidification Behavior and Grain Morphology of Laser Additive Manufacturing Titanium Alloys," *J. Alloys. Compd.*, **777**, pp. 712–716.
- [22] Dong, W., Liang, X., Chen, Q., Hinnebusch, S., Zhou, Z., and To, A. C., 2021, "A New Procedure for Implementing the Modified Inherent Strain Method With Improved Accuracy in Predicting Both Residual Stress and Deformation for Laser Powder Bed Fusion," *Addit. Manuf.*, **47**, p. 102345.
- [23] Megahed, M., Mindt, H.-W., Willems, J., Dionne, P., Jacquemetton, L., Craig, J., Ranade, P., and Peralta, A., 2019, "LPBF Right the First Time the Right Mix Between Modeling and Experiments," *Int. Mater. Manuf. Innovat.*, **8**(2), pp. 194–216.
- [24] King, W. E., Anderson, A. T., Ferencz, R. M., Hodge, N. E., Kamath, C., Khairallah, S. A., and Rubenchik, A. M., 2015, "Laser Powder Bed Fusion

- Additive Manufacturing of Metals; Physics, Computational, and Materials Challenges," *Appl. Phys. Rev.*, **2**(4), p. 041304.
- [25] Mozaffar, M., Liao, S., Jeong, J., Xue, T., and Cao, J., 2023, "Differentiable Simulation for Material Thermal Response Design in Additive Manufacturing Processes," *Addit. Manuf.*, **61**, p. 103337.
 - [26] Sun, Z., Ma, Y., Ponge, D., Zaefferer, S., Jäggle, E. A., Gault, B., Rollett, A. D., and Raabe, D., 2022, "Thermodynamics-Guided Alloy and Process Design for Additive Manufacturing," *Nat. Commun.*, **13**(1), pp. 1–12.
 - [27] Mahmoud, D., Magolon, M., Boer, J., Elbestawi, M., and Mohammadi, M. G., 2021, "Applications of Machine Learning in Process Monitoring and Controls of L-PBF Additive Manufacturing: A Review," *Appl. Sci.*, **11**(24), p. 11910.
 - [28] AbouelNour, Y., and Gupta, N., 2022, "In-Situ Monitoring of Sub-surface and Internal Defects in Additive Manufacturing: A Review," *Mater. Design*, **222**, p. 111063.
 - [29] Gu, G. X., Chen, C.-T., Richmond, D. J., and Buehler, M. J., 2018, "Bioinspired Hierarchical Composite Design Using Machine Learning: Simulation, Additive Manufacturing, and Experiment," *Mater. Horiz.*, **5**(5), pp. 939–945.
 - [30] Wang, R., and Behandish, M., 2022, "Surrogate Modeling for Physical Systems With Preserved Properties and Adjustable Tradeoffs," Preprint arXiv:2202.01139.
 - [31] Stathatos, E., and Vosniakos, G.-C., 2019, "Real-Time Simulation for Long Paths in Laser-Based Additive Manufacturing: A Machine Learning Approach," *Int. J. Adv. Manuf. Technol.*, **104**(5), pp. 1967–1984.
 - [32] Zhu, Q., Liu, Z., and Yan, J., 2021, "Machine Learning for Metal Additive Manufacturing: Predicting Temperature and Melt Pool Fluid Dynamics Using Physics-Informed Neural Networks," *Comput. Mech.*, **67**(2), pp. 619–635.
 - [33] Kats, D., Wang, Z., Gan, Z., Liu, W. K., Wagner, G. J., and Lian, Y., 2022, "A Physics-Informed Machine Learning Method for Predicting Grain Structure Characteristics in Directed Energy Deposition," *Comput. Mater. Sci.*, **202**, p. 110958.
 - [34] Karniadakis, G. E., Kevrekidis, I. G., Lu, L., Perdikaris, P., Wang, S., and Yang, L., 2021, "Physics-Informed Machine Learning," *Nat. Rev. Phys.*, **3**(6), pp. 422–440.
 - [35] Elhamod, M., Bu, J., Singh, C., Redell, M., Ghosh, A., Podolskiy, V., Lee, W.-C., and Karpatne, A., 2022, "CoPhy-PGNN: Learning Physics-Guided Neural Networks With Competing Loss Functions for Solving Eigenvalue Problems," *ACM Trans. Intel. Syst. Technol.*, **13**(6), pp. 1–23.
 - [36] Raissi, M., Perdikaris, P., and Karniadakis, G. E., 2019, "Physics-Informed Neural Networks: A Deep Learning Framework for Solving Forward and Inverse Problems Involving Nonlinear Partial Differential Equations," *J. Comput. Phys.*, **378**, pp. 686–707.
 - [37] Shin, Y., Darbon, J., and Karniadakis, G. E., 2020, "On the Convergence of Physics Informed Neural Networks for Linear Second-Order Elliptic and Parabolic Type PDEs," *Commun. Comput. Phys.*, **28**(5), pp. 2042–2074.
 - [38] Sing, S., Kuo, C., Shih, C., Ho, C., and Chua, C., 2021, "Perspectives of Using Machine Learning in Laser Powder Bed Fusion for Metal Additive Manufacturing," *Virtual Phys. Protot.*, **16**(3), pp. 372–386.
 - [39] Robbins, J., Owen, S., Clark, B., and Voth, T., 2016, "An Efficient and Scalable Approach for Generating Topologically Optimized Cellular Structures for Additive Manufacturing," *Addit. Manuf.*, **12**, pp. 296–304.
 - [40] Hassanin, H., Alkendi, Y., Elsayed, M., Essa, K., and Zweiri, Y., 2020, "Controlling the Properties of Additively Manufactured Cellular Structures Using Machine Learning Approaches," *Adv. Eng. Mater.*, **22**(3), p. 1901338.
 - [41] Rastegarzadeh, S., Wang, J., and Huang, J., 2023, "Neural Network-Assisted Design: A Study of Multiscale Topology Optimization With Smoothly Graded Cellular Structures," *ASME J. Mech. Des.*, **145**(1), p. 011701.
 - [42] Williams, G., Meisel, N. A., Simpson, T. W., and McComb, C., 2019, "Design Repository Effectiveness for 3d Convolutional Neural Networks: Application to Additive Manufacturing," *ASME J. Mech. Des.*, **141**(11), p. 111701.
 - [43] Zhang, Y., Dong, G., Yang, S., and Zhao, Y. F., 2019, "Machine Learning Assisted Prediction of the Manufacturability of Laser-Based Powder Bed Fusion Process," International Design Engineering Technical Conferences and Computers and Information in Engineering Conference, Anaheim, CA, Aug. 18–21, Vol. 59179, American Society of Mechanical Engineers, p. V001T02A008.
 - [44] Whitt, A., Seede, R., Ye, J., Elverud, M., Vaughan, M., Elwany, A., Arroyave, R., and Karaman, I., 2023, "A Process Optimization Framework for Laser Direct Energy Deposition: Densification, Microstructure, and Mechanical Properties of an FCC Alloy," *J. Manuf. Proc.*, **85**, pp. 434–449.
 - [45] Wang, P., Yang, Y., and Moghaddam, N. S., 2022, "Process Modeling in Laser Powder Bed Fusion Towards Defect Detection and Quality Control Via Machine Learning: The State-of-the-Art and Research Challenges," *J. Manuf. Proc.*, **73**, pp. 961–984.
 - [46] Fu, Y., Downey, A. R., Yuan, L., Zhang, T., Pratt, A., and Balogun, Y., 2022, "Machine Learning Algorithms for Defect Detection in Metal Laser-Based Additive Manufacturing: A Review," *J. Manuf. Proc.*, **75**, pp. 693–710.
 - [47] Yang, Z., Lu, Y., Yeung, H., and Kirshnamurthy, S., 2020, "3d Build Melt Pool Predictive Modeling for Powder Bed Fusion Additive Manufacturing," International Design Engineering Technical Conferences and Computers and Information in Engineering Conference, Virtual, Online, Aug. 17–19, Vol. 83983, American Society of Mechanical Engineers, p. V009T09A046.
 - [48] Kwon, O., Kim, H. G., Kim, W., Kim, G.-H., and Kim, K., 2020, "A Convolutional Neural Network for Prediction of Laser Power Using Melt-Pool Images in Laser Powder Bed Fusion," *IEEE Access*, **8**, pp. 23255–23263.
 - [49] Bugatti, M., and Colosimo, B. M., 2022, "Towards Real-Time In-Situ Monitoring of Hot-Spot Defects in L-PBF: A New Classification-Based Method for Fast Video-Imaging Data Analysis," *J. Intell. Manuf.*, **33**(1), pp. 293–309.
 - [50] Ren, Y., and Wang, Q., 2020, "Physics-Informed Gaussian Process Based Optimal Control of Laser Powder Bed Fusion," Dynamic Systems and Control Conference, Virtual, Online, Oct. 5–7, Vol. 84287, American Society of Mechanical Engineers, p. V002T24A001.
 - [51] Ren, Y., Wang, Q., and Michaleris, P., 2019, "Machine-Learning Based Thermal-Geometric Predictive Modeling of Laser Powder Bed Fusion Additive Manufacturing," Dynamic Systems and Control Conference, Park City, UT, Oct. 8–11, Vol. 59148, American Society of Mechanical Engineers, p. V001T10A001.
 - [52] Moges, T., Yang, Z., Jones, K., Feng, S., Witherell, P., and Lu, Y., 2021, "Hybrid Modeling Approach for Melt-Pool Prediction in Laser Powder Bed Fusion Additive Manufacturing," *ASME J. Comput. Inf. Sci. Eng.*, **21**(5), p. 050902.
 - [53] Smoqi, Z., Gaikwad, A., Bevans, B., Kobir, M. H., Craig, J., Abul-Haj, A., Peralta, A., and Rao, P., 2022, "Monitoring and Prediction of Porosity in Laser Powder Bed Fusion Using Physics-Informed Meltpool Signatures and Machine Learning," *J. Mater. Process. Technol.*, **304**, p. 117550.
 - [54] Vela, B., Mehalic, S., Sheikh, S., Elwany, A., Karaman, I., and Arróyave, R., 2022, "Evaluating the Intrinsic Resistance to Balling of Alloys: A High-Throughput Physics-Informed and Data-Enabled Approach," *Additive Manuf. Lett.*, **3**, p. 100085.
 - [55] Wang, Y., Yao, Q., Kwok, J. T., and Ni, L. M., 2020, "Generalizing From a Few Examples: A Survey on Few-Shot Learning," *ACM Comput. Surveys (csur)*, **53**(3), pp. 1–34.
 - [56] Raissi, M., Perdikaris, P., and Karniadakis, G. E., 2017, "Physics Informed Deep Learning (Part i): Data-Driven Solutions of Nonlinear Partial Differential Equations," Preprint arXiv:1711.10561.
 - [57] Liao, S., Xue, T., Jeong, J., Webster, S., Ehmann, K., and Cao, J., 2023, "Hybrid Thermal Modeling of Additive Manufacturing Processes Using Physics-Informed Neural Networks for Temperature Prediction and Parameter Identification," *Comput. Mech.*, **72**(1), pp. 499–512.
 - [58] Silvestri, M., Lombardi, M., and Milano, M., 2021, "Injecting Domain Knowledge in Neural Networks: A Controlled Experiment on a Constrained Problem," International Conference on Integration of Constraint Programming, Vienna, Austria, July 5–8, Springer, pp. 266–282.
 - [59] Jin, X., Cai, S., Li, H., and Karniadakis, G. E., 2021, "Nsfnets (Navier-Stokes Flow Nets): Physics-Informed Neural Networks for the Incompressible Navier-Stokes Equations," *J. Comput. Phys.*, **426**, p. 109951.
 - [60] Yang, Y., and Perdikaris, P., 2019, "Adversarial Uncertainty Quantification in Physics-Informed Neural Networks," *J. Comput. Phys.*, **394**, pp. 136–152.
 - [61] Meng, X., Li, Z., Zhang, D., and Karniadakis, G. E., 2020, "Ppinn: Parareal Physics-Informed Neural Network for Time-Dependent PDEs," *Comput. Methods. Appl. Mech. Eng.*, **370**, p. 113250.
 - [62] Kharazmi, E., Zhang, Z., and Karniadakis, G. E., 2019, "Variational Physics-Informed Neural Networks for Solving Partial Differential Equations," Preprint arXiv:1912.00873.
 - [63] Li, M., and McComb, C., 2022, "Using Physics-Informed Generative Adversarial Networks to Perform Super-Resolution for Multiphase Fluid Simulations," *ASME J. Comput. Inf. Sci. Eng.*, **22**(4), p. 044501.
 - [64] Noakoosteen, O., Wang, S., Peng, Z., and Christodoulou, C., 2020, "Physics-Informed Deep Neural Networks for Transient Electromagnetic Analysis," *IEEE Open J. Antennas Propagation*, **1**, pp. 404–412.
 - [65] Liu, D., and Wang, Y., 2019, "Multi-fidelity Physics-Constrained Neural Network and Its Application in Materials Modeling," *ASME J. Mech. Des.*, **141**(12), p. 121403.
 - [66] Stockman, T., Schneider, J. A., Walker, B., and Carpenter, J. S., 2019, "A 3d Finite Difference Thermal Model Tailored for Additive Manufacturing," *Jom*, **71**(3), pp. 1117–1126.
 - [67] Shen, N., and Chou, K., 2012, "Thermal Modeling of Electron Beam Additive Manufacturing Process: Powder Sintering Effects," International Manufacturing Science and Engineering Conference, Notre Dame, IN, June 4–8, pp. 287–295.
 - [68] Roberts, I. A., Wang, C., Esterlein, R., Stanford, M., and Mynors, D., 2009, "A Three-Dimensional Finite Element Analysis of the Temperature Field During Laser Melting of Metal Powders in Additive Layer Manufacturing," *Int. J. Mach. Tools. Manuf.*, **49**(12–13), pp. 916–923.
 - [69] Zhang, Z., Huang, Y., Kasinathan, A. R., Shahabad, S. I., Ali, U., Mahmoodkhani, Y., and Toyserkani, E., 2019, "3-Dimensional Heat Transfer Modeling for Laser Powder-Bed Fusion Additive Manufacturing With Volumetric Heat Sources Based on Varied Thermal Conductivity and Absorptivity," *Optics Laser Tech.*, **109**, pp. 297–312.
 - [70] Tan, M., and Le, Q., 2019, "EfficientNet: Rethinking Model Scaling for Convolutional Neural Networks," International Conference on Machine Learning, Long Beach, CA, June 9–15, PMLR, pp. 6105–6114.
 - [71] Slotwinski, J. A., Garboczi, E. J., Stutzman, P. E., Ferraris, C. F., Watson, S. S., and Peltz, M. A., 2014, "Characterization of Metal Powders Used for Additive Manufacturing," *J. Res. Natl. Inst. Stand. Technol.*, **119**(1), p. 460.
 - [72] Masoomi, M., Soltani-Tehrani, A., Shamsaei, N., and Thompson, S. M., 2018, "Convection Heat Transfer Coefficients for Laser Powder Bed Fusion," 2018 International Solid Freeform Fabrication Symposium, Austin, TX, Aug. 13–15.
 - [73] Ripetskiy, A., Zelenov, S., Kuznetsova, E., and Rabinskiy, L., 2018, "Evaluation of the Thermal Processes and Simulation Methods for Additive Manufacturing Based on the Geometry Voxel Representation," *Key Engineering Materials*, **771**(1), pp. 91–96.

- [74] Ladani, L., Romano, J., Brindley, W., and Burlatsky, S., 2017, "Effective Liquid Conductivity for Improved Simulation of Thermal Transport in Laser Beam Melting Powder Bed Technology," *Addit. Manuf.*, **14**, pp. 13–23.
- [75] Buchmayr, B., Panzl, G., Walzl, A., and Wallis, C., 2017, "Laser Powder Bed Fusion—Materials Issues and Optimized Processing Parameters for Tool Steels, AlSiMg-and CuCrZr-Alloys," *Adv. Eng. Mater.*, **19**(4), p. 1600667.
- [76] Ninpetch, P., Kowitwarangkul, P., Mahathanabodee, S., Tongsri, R., and Ratanadecho, P., 2019, "Thermal and Melting Track Simulations of Laser Powder Bed Fusion (L-PBF)," IOP Conference Series: Materials Science and Engineering, Bangkok, Thailand, Dec. 17–21, Vol. 526, IOP Publishing, p. 012030.
- [77] Woolson, R. F., 2007, "Wilcoxon Signed-Rank Test," *Wiley Encyclopedia of Clinical Trials*, pp. 1–3.
- [78] Oyeka, I. C. A., and Ebuh, G. U., 2012, "Modified Wilcoxon Signed-Rank Test," *Open J. Stat.*, **2**(2), pp. 172–176.
- [79] Durango, A., and Refugio, C., 2018, "An Empirical Study on Wilcoxon Signed Rank Test," *J. Negros Orient. State Univ.*, **8**(8), pp. 130–136.
- [80] Pierce, J., Williams, G., Simpson, T. W., Meisel, N. A., and McComb, C., 2021, "Stochastically Trained Physics-Informed Neural Networks: Application to Thermal Analysis in Metal Laser Powder Bed Fusion," International Design Engineering Technical Conferences and Computers and Information in Engineering Conference, Virtual, Online, Aug. 17–19, Vol. 85383, American Society of Mechanical Engineers, p. V03AT03A004.